



CHORUS

This is the accepted manuscript made available via CHORUS. The article has been published as:

Meron, skyrmion, and vortex crystals in centrosymmetric tetragonal magnets

Zhentao Wang, Ying Su, Shi-Zeng Lin, and Cristian D. Batista

Phys. Rev. B **103**, 104408 — Published 4 March 2021

DOI: [10.1103/PhysRevB.103.104408](https://doi.org/10.1103/PhysRevB.103.104408)

Meron, skyrmion, and vortex crystals in centrosymmetric tetragonal magnets

Zhentaο Wang,^{1,2} Ying Su,³ Shi-Zeng Lin,³ and Cristian D. Batista^{1,4}

¹*Department of Physics and Astronomy, The University of Tennessee, Knoxville, Tennessee 37996, USA*

²*School of Physics and Astronomy, University of Minnesota, Minneapolis, Minnesota 55455, USA*

³*Theoretical Division, T-4 and CNLS, Los Alamos National Laboratory, Los Alamos, New Mexico 87545, USA*

⁴*Neutron Scattering Division and Shull-Wollan Center,*

Oak Ridge National Laboratory, Oak Ridge, Tennessee 37831, USA

(Dated: February 16, 2021)

The recent experimental confirmation of a transformation between meron and skyrmion topological spin textures in the chiral magnet $\text{Co}_2\text{Zn}_9\text{Mn}_3$ [S.-Z. Lin et al., Phys. Rev. B 91, 224407 (2015); X. Z. Yu et al., Nature 564, 95 (2018)] confirms that the skyrmion crystals discovered in 2009 [S. Mühlbauer et al., Science 323, 915 (2009)] are just the tip of the iceberg. Crystals of topological textures, including skyrmions, merons, vortices and monopoles can be stabilized by combining simple physical ingredients, such as lattice symmetry, frustration and spin anisotropy. The current challenge is to find the combinations of these ingredients that produce specific topological spin textures. Here we report a simple mechanism for the stabilization of meron, skyrmion, and vortex crystals in centrosymmetric tetragonal magnets. In particular, the meron/skyrmion crystals can form even in absence of magnetic field. The application of magnetic field leads to a rich variety of novel topological spin textures that survive in the long wavelength limit of the theory. When conduction electrons are coupled to the spins, these topological spin textures twist the electronic wave functions to induce Chern insulators and Weyl semimetals for specific band filling fractions.

PACS numbers:

I. INTRODUCTION

Inspired by the work of Herman Hemholtz [1], William Thompson proposed in 1867 that atoms could be vortices in ether [2]. While later experiments put this proposal out of business, thinking of topological solitons as emerging building blocks or artificial atoms is very appealing. Indeed, more recent developments, that started around the 1960's [3, 4], have demonstrated that nature has plenty of room for finding updated versions of ether [5]. The “ether of quantum magnets” is the vector field of magnetic moments, whose topological solitons can be regarded as emergent mesoscale atoms [6]. Like real atoms, these solitons form crystal structures dictated by symmetry, anisotropy and competing interactions.

Periodic arrays of topological spin textures typically arise from the superposition of small- \mathbf{Q} spirals propagating along symmetry related directions (multi- \mathbf{Q} ordering), whose wavelength is dictated by the competition between ferromagnetic (FM) and antiferromagnetic (AFM) interactions. In chiral magnets, the FM interaction competes against the antisymmetric component of the effective exchange tensor, known as Dzyaloshinskii-Moriya (DM) interaction [7, 8]. However, the selection of a small- \mathbf{Q} spiral ordering is not enough to stabilize topological spin textures because the superposition of multiple spirals requires additional energetic considerations. For instance, it is known that three-fold symmetric lattices favor the formation of skyrmion crystals (triple- \mathbf{Q} ordering) induced by a magnetic field parallel to the c -axis, because the Ginzburg-Landau (GL) free energy can include terms of the form $(\mathbf{S}_0 \cdot \mathbf{S}_{\mathbf{Q}_1})(\mathbf{S}_{\mathbf{Q}_2} \cdot \mathbf{S}_{\mathbf{Q}_3})$ ($\mathbf{Q}_1 + \mathbf{Q}_2 + \mathbf{Q}_3 = 0$ because the three ordering wavevectors differ by $2\pi/3$ rotations). This simple consideration explains why the vast majority of magnetic skyrmion crystals have been found by applying magnetic field along a *three-fold* symmetry axis of different materials [9].

While less common, square skyrmion and meron crystals have been recently reported in chiral [10–12], polar [13, 14], and centrosymmetric tetragonal magnets [15]. The observation of skyrmion crystals in four-fold symmetric lattices forces us to think about alternative stabilization mechanisms. Here, we report a new guiding principle for the formation of meron crystals (MX), which are also skyrmion crystals (SkX), in four-fold (tetragonal) lattices *even in absence of magnetic field*. The merons form a square lattice and the magnetic unit cell includes four merons with a net skyrmion charge $n_{\text{sk}} = \pm 1$ (MX-I) or $n_{\text{sk}} = \pm 2$ (MX-II). The phase diagram also includes a field-induced vortex crystal (VtX). Remarkably, this rich phase diagram is obtained from a very simple model for centrosymmetric magnets that only includes competing easy-axis and compass anisotropies.

The different phases of the phase diagram are obtained by minimizing the energy over all the possible spin configurations for a fixed magnetic unit cell, whose size is dictated by the ordering wavevector. We also provide approximated expansions of the relevant spin configurations that include the fundamental Fourier components $\mathbf{q} = \mathbf{Q}_\nu$ and a few higher harmonics. Our analysis is complemented with the derivation of the GL theory that describes the long wavelength limit of the microscopic model, allowing us to demonstrate the universal character of the phase diagram. We also analyze the anomalous Hall response of itinerant electrons coupled to the local magnetic moments [16], and the possible realization a magnetic Weyl semimetal [17] induced by the MX-II phase.

The rest of paper is organized as follows: in Sec. II we introduce the microscopic model and compute the corresponding $T = 0$ phase diagrams. In Sec. III we introduce a Ginzburg-Landau theory for the continuum limit of the model, and discuss the stabilization condition of the MX-II phase. In Sec. IV we analyze the topological Hall effect that results

from coupling the MX-I and MX-II spin textures to conduction electrons. In Sec. V we discuss the generation of Weyl points in vertically stacked layers of MX-II spin textures. In Sec. VI we summarize the main conclusions of the work. Appendix A provides details of the variational methods that were employed to obtain the $T = 0$ phase diagrams. Appendix B includes the analysis of the ordering wavevectors in the isotropic limit of the model. A further analysis of the skyrmion charge in the meron crystal phases is provided in Appendix C. Appendix D includes the Fourier analysis of the states that were obtained from the unbiased (fixed unit cell) variational method. Appendix E includes details of the stability analysis of the MX-II phase. Finally, we present the symmetry analysis of the electronic bands in Appendix F.

II. MICROSCOPIC MODEL

We consider the *classical* Heisenberg model on the square lattice:

$$\mathcal{H} = \sum_{\langle ij \rangle} J_{ij} \mathbf{S}_i \cdot \mathbf{S}_j - \Gamma \sum_i \left(S_i^x S_{i+\hat{x}}^x + S_i^y S_{i+\hat{y}}^y \right) - D \sum_i (S_i^z)^2 - H \sum_i S_i^z, \quad (1)$$

where $J_{ij} = \{J_1, J_2, J_3\}$ are the Heisenberg interactions up to the third nearest neighbor, Γ is the compass anisotropy, D is the single-ion anisotropy, and H is the magnetic field along the z -axis. In this work, we consider the case of FM nearest neighbor Heisenberg exchange ($J_1 < 0$). The magnitude of the spins is fixed by the normalization condition $|\mathbf{S}_i| = 1$. The compass anisotropy can either be generated by the spin-orbit coupling or by the dipolar interaction.

The characteristic length scale of the spin structure is determined by the competition between different symmetric exchange interactions [18–23]. In absence of anisotropies and magnetic field, the ordering wavevector \mathbf{Q} is obtained by minimizing the exchange interaction in momentum space:

$$J(\mathbf{q}) = J_1 (\cos q_x + \cos q_y) + 2J_2 \cos q_x \cos q_y + J_3 (\cos 2q_x + \cos 2q_y). \quad (2)$$

In the long wavelength limit we have:

$$J(\mathbf{q}) \simeq I_0 - \frac{I_1}{2} q^2 + \frac{I_2}{2} q^4 - I_3 q_x^2 q_y^2, \quad (3)$$

with $I_0 = 2(J_1 + J_2 + J_3)$ and

$$I_1 = J_1 + 2J_2 + 4J_3, \quad I_2 = \frac{J_1 + 2J_2 + 16J_3}{12}, \quad I_3 = I_2 - \frac{J_2}{2}. \quad (4)$$

Depending on the sign of the quartic anisotropy, I_3 , the competing exchange interactions lead to spiral phases with ordering wavevectors $\mathbf{Q} = (\pm Q_0, 0)$ or $\mathbf{Q} = (0, \pm Q_0)$ with $Q_0 = \sqrt{I_1/2I_2}$ for $I_3 < 0$, and $\mathbf{Q} = (\pm Q_0, \pm Q_0)/\sqrt{2}$ with $Q_0 = \sqrt{I_1/(2I_2 - I_3)}$ for $I_3 > 0$ ¹. In **both situations**, the ground state can either

be a single- \mathbf{Q} spiral or a multi- \mathbf{Q} structure depending on the values of the spin anisotropies and the magnetic field. Once these extra terms are included in the Hamiltonian, the optimal value of \mathbf{Q} can also change. We note, however, that this change has been found to be negligible for several cases of interest [19, 24].

The different rows of Fig. 1 include the $T = 0$ phase diagrams of \mathcal{H} for three different sets of exchange interactions, $\{J_1, J_2, J_3\}$ that produce relatively small values of Q and quartic anisotropy: $I_3 = 0.02|J_1|$, $I_3 = 0$ and $I_3 \approx -0.037|J_1|$. The different columns correspond to four different values of the compass anisotropy Γ . As shown in Fig. 2, the inclusion of these extra terms indeed modifies ordering wavenumber.

Since I_3 and Γ are the main sources of tetragonal anisotropy, the first column of Fig. 1 [Figs. 1(a)(e)(i)] describes cases with weak lattice anisotropy. Thus, it is not surprising that the phase diagrams are similar to the ones obtained in the continuum limit of the *isotropic theory* [20]. The ordering wavevectors $\{\mathbf{Q}_1, \mathbf{Q}_2, \mathbf{Q}_3\}$ differ by 120° , implying that the skyrmion crystal SkX(Δ) has hexagonal symmetry in spite of the underlying tetragonal atomic lattice. The conical spiral (CS) is just a canted cycloidal spiral induced by the effective easy-plane anisotropy produced by the applied magnetic field. In contrast, the easy-axis anisotropy term $D > 0$ favors a proper-screw or vertical spiral (VS). The additional two phases, $2\mathbf{Q}$ -conical spiral [$2\mathbf{Q}$ -CS(Δ)]², and the vertical spiral with in-plane modulation [VS'(Δ)] have also been reported for centrosymmetric magnets with hexagonal symmetry [18–22, 24].

The phase diagram is qualitatively different for $\Gamma/|J_1| \geq 0.1$ because the compass anisotropy term is strong enough to enforce the tetragonal anisotropy on the spin textures. The propagation wavevectors, $\mathbf{Q}_1 = (Q, 0)$ and $\mathbf{Q}_2 = (0, Q)$ of the conical and the vertical spirals are now pinned along the principal x and y directions of the tetragonal lattice³. However, the most remarkable effect of the Γ -term is the stabilization of double- \mathbf{Q} orderings that are superpositions of two proper screw spirals with propagation wavevectors \mathbf{Q}_1 and \mathbf{Q}_2 . In particular, the MX-II, MX-I and VtX phases, shown in Figs. 3(a)–(c), have the same intensity in the spin structure factor at both wavevectors; while the vertical spiral with in-plane modulation (VS') has different intensities [Fig. 3(d)], implying that it is not invariant under a 90 degree rotation.

The magnetic unit cell of the MX-II state includes four merons [Fig. 3(a)], whose skyrmion charge adds up to $|n_{\text{sk}}| = 2$ [Fig. 3(a), Fig. 8(a)], meaning that the MX-II phase is simultaneously a double-SkX state with net scalar spin chirality $\chi_{ijk} = \mathbf{S}_i \cdot (\mathbf{S}_j \times \mathbf{S}_k)$. Note that the scalar chiralities of the merons have the same sign because a change of sign in the vector spin chirality $\hat{z} \cdot (\mathbf{S}_j \times \mathbf{S}_k)$ (vorticity) is always accompanied by a sign change of S_i^z . The MX-I phase is induced by magnetic field, but it can also exist at zero magnetic field

¹ Such analysis is valid in the long wavelength limit. The corrections for finite $|\mathbf{Q}|$ can be found in Appendix B.

² The name $2\mathbf{Q}$ -CS(Δ) follows the convention of refs. [19, 24], where $S(\mathbf{q})$ actually has intensity at all $\{\mathbf{Q}_1, \mathbf{Q}_2, \mathbf{Q}_3\}$, but the spectral weight at the third \mathbf{Q} can be quite small compared to the other two.

³ Note also that a new $\uparrow\uparrow\downarrow$ state appears for large enough anisotropy [see Fig. 1(l)].

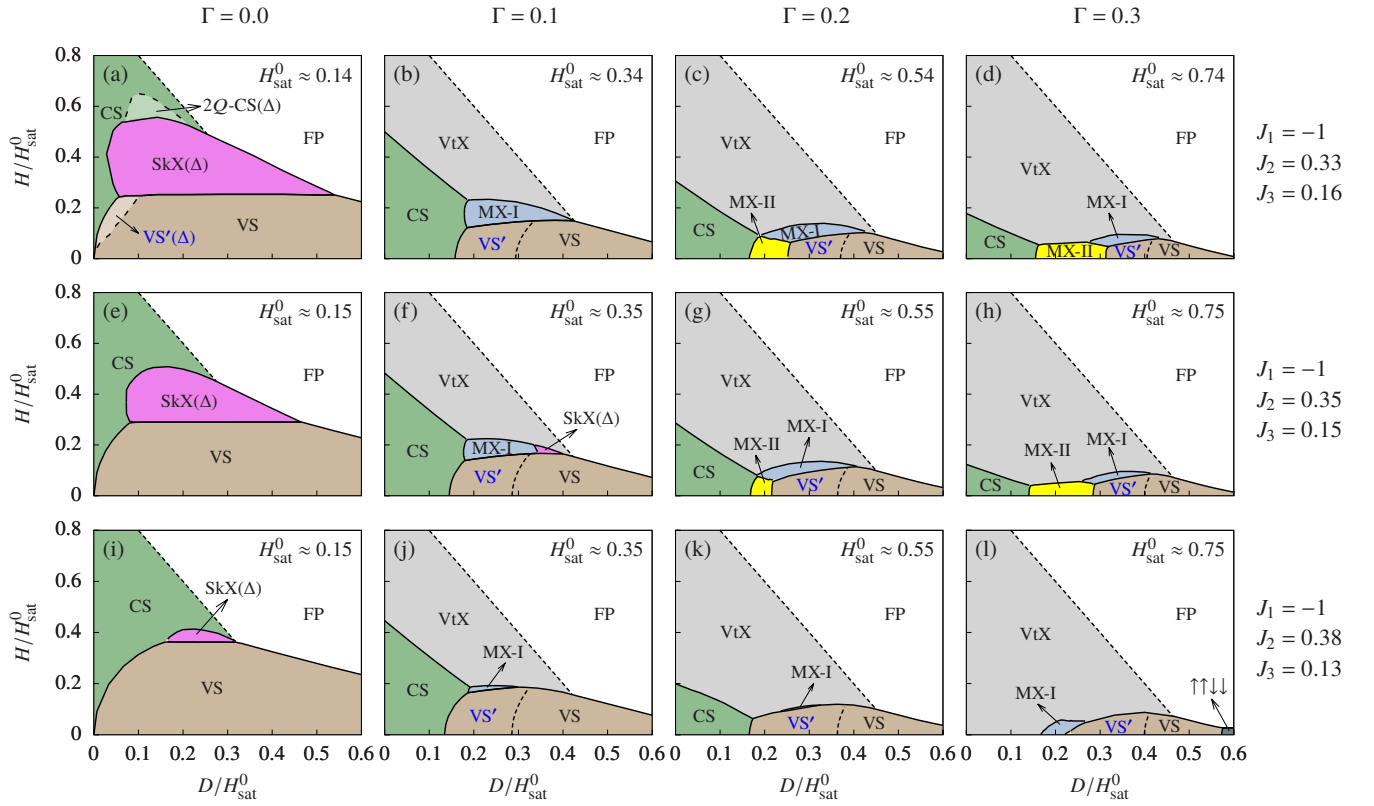


Figure 1. Phase diagrams of the microscopic model Eq. (1) at $T = 0$. The values of $\{J_1, J_2, J_3\}$ are denoted on the right-hand side of each row (see also Fig. 7), and the values of Γ are denoted on top of each column. **The solid (dashed) lines indicate first (second) order phase transitions.**

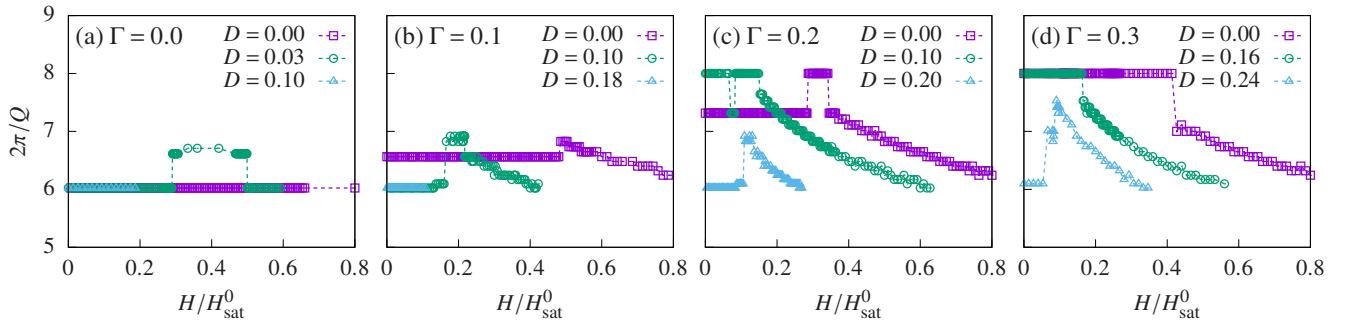


Figure 2. Wavelength of the spin textures obtained from the microscopic model Eq. (1) at $T = 0$ (see Appendix A for details). Here we set $J_1 = -1$, $J_2 = 0.35$, $J_3 = 0.15$, and the values of H_{sat}^0 are denoted on the corresponding panels in Fig. 1. Note that some of the points have a small error bar, which can be inferred from the noise of the corresponding curves, because of the limited resolution of the minimization algorithm.

[Fig. 1(l)]. Its magnetic unit cell includes four merons with a total skyrmion charge $|n_{\text{sk}}| = 1$ [Fig. 3(b), Fig. 8(b)], implying that this phase is also a SkX. In this case, one of the merons has opposite scalar chirality relative to the other three because of a sign change in S_i^z near its core. It is interesting to note that the MX-I state is topologically equivalent to the spin configurations that have been observed in chiral crystals [Fig. 1(e) of ref. [12]] and centrosymmetric magnets [Fig. 1(d) of ref. [15]]. The finite skyrmion charges of the MX-I and MX-II phases make them qualitatively different from the MXs

with $n_{\text{sk}} = 0$ that have been reported in previous works [25, 26].

The VtX state can in principle exist all the way from zero magnetic field up to the saturation (Fig. 1). Similarly to the MX-I and MX-II states, this texture includes four vortices in each magnetic unit cell. The main difference is that their topological charges cancel with each other: $n_{\text{sk}} = 0$ [Fig. 3(c), Fig. 8(c)]. The origin of this cancellation is easy to understand at high fields, where S_i^z does not change sign and the net scalar chirality becomes proportional to the net vector chirality. Hexagonal versions of this VtX phase have also been reported

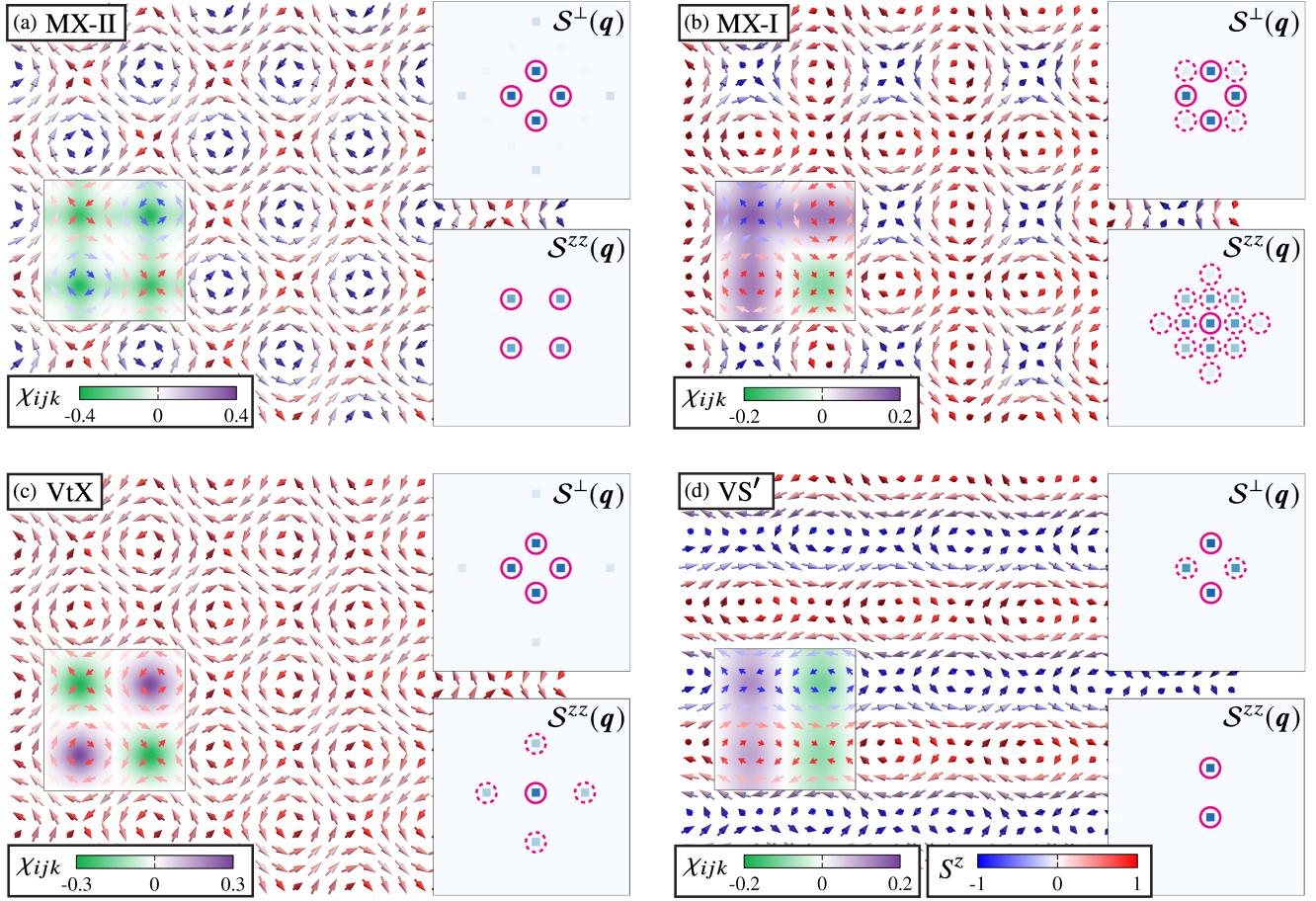


Figure 3. Spin configurations of the double- \mathbf{Q} states. The insets show the in-plane (S^\perp) and out-of-plane (S^{zz}) static spin structure factors in the first BZ (the intensities are colored in log scale). The solid (dotted) circles highlight the dominant (subdominant) peaks for $q \leq 2Q$. On the left part of each panel, we have also colored the scalar chirality χ_{ijk} in the magnetic unit cell.

for frustrated *quantum* magnets below the saturation field [27, 28].

The in-plane spin components are almost *identical* for the MX-I, MX-II, and VtX states [Figs. 3(a)–(c)], making them equally good candidates for the double- \mathbf{Q} magnetic textures revealed by Lorentz transmission electron microscopy (TEM) [12, 15]. We must then rely on other measurements to discriminate between the three possibilities. As shown in Figs. 3(a)–(c), the zz component of the static spin structure factor, $S^{zz}(\mathbf{q})$, is different for the three double- \mathbf{Q} orderings. In other words, a polarized neutron or x-ray diffraction experiment can identify the nature the double- \mathbf{Q} state. We also note that $S(\mathbf{Q}_1 + \mathbf{Q}_2) \approx 0$ for the VtX state [Fig. 3(c)], meaning that the spectral weight at the first harmonic, $\mathbf{Q}_1 + \mathbf{Q}_2$, is not always a good criterion to distinguish a multi-domain single- \mathbf{Q} phase from a double- \mathbf{Q} state. Recently, a double- \mathbf{Q} state has been reported in the centrosymmetric tetragonal magnet GdRu_2Si_2 [15], which has substantial weight at the higher harmonic position $\mathbf{Q}_1 + \mathbf{Q}_2$. This observation excludes the VtX, but it is still consistent with the MX-I or MX-II phases.

III. GINZBURG-LANDAU THEORY

The universal GL theory ($Q \rightarrow 0$) is obtained via the gradient expansion

$$\mathbf{S}_{\mathbf{r}+\delta} \approx \mathbf{S}_{\mathbf{r}} + (\delta \cdot \nabla) \mathbf{S}_{\mathbf{r}} + \frac{1}{2} (\delta \cdot \nabla)^2 \mathbf{S}_{\mathbf{r}} + \dots, \quad (5)$$

that leads to the continuum version of Eq. (1):

$$\begin{aligned} \mathcal{H}_{\text{GL}} = \int d\mathbf{r} \left\{ -\frac{I_1}{2} \left[(\partial_x \mathbf{S}_{\mathbf{r}})^2 + (\partial_y \mathbf{S}_{\mathbf{r}})^2 \right] \right. \\ \left. + \frac{I_2}{2} \left(\partial_x^2 \mathbf{S}_{\mathbf{r}} + \partial_y^2 \mathbf{S}_{\mathbf{r}} \right)^2 + \frac{\Gamma}{2} \left[(\partial_x S_r^x)^2 + (\partial_y S_r^y)^2 \right] \right. \\ \left. - (D - \Gamma) (S_r^z)^2 - H S_r^z - I_3 \left(\partial_x^2 \mathbf{S}_{\mathbf{r}} \right) \cdot \left(\partial_y^2 \mathbf{S}_{\mathbf{r}} \right) \right\}. \quad (6) \end{aligned}$$

The compass anisotropy and the last term of Eq. (6) are the only terms of \mathcal{H}_{GL} that enforce the C_4 anisotropy of the original lattice model. In agreement with the phase diagram of the microscopic model, the quartic exchange anisotropy penalizes multi- \mathbf{Q} states for $I_3 < 0$ (bottom row of Fig. 1), while it favors them for $I_3 > 0$ (top row of Fig. 1). This point

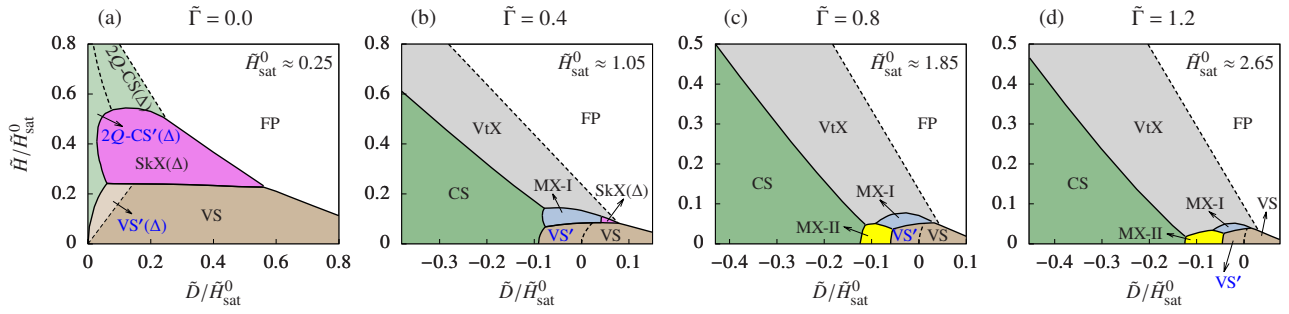


Figure 4. Phase diagrams of the GL theory Eq. (9) with $I_3 = 0$ at $T = 0$. The values of $\tilde{\Gamma}$ are denoted on the top of each column. The solid (dashed) lines indicate first (second) order phase transitions.

becomes clearer upon taking the Fourier transform of the I_3 term:

$$-I_3 \int d\mathbf{q} \left(q_x^2 q_y^2 \right) \mathbf{S}_{\mathbf{q}} \cdot \mathbf{S}_{-\mathbf{q}}. \quad (7)$$

The characteristic wavelength of the ground state is set by the length scale $\sqrt{I_2/I_1}$. By adopting this scale as the unit of length $\mathbf{r} \rightarrow \sqrt{I_1/I_2} \mathbf{r}$, I_1 as the unit of energy and I_1^2/I_2 as the unit of magnetic field, the GL energy functional Eq. (6) can be re-expressed in terms of the dimensionless coupling constants,

$$\tilde{\Gamma} \equiv \frac{\Gamma}{I_1}, \quad \tilde{D} \equiv \frac{I_2(D-\Gamma)}{I_1^2}, \quad \tilde{H} \equiv \frac{I_2 H}{I_1^2}, \quad \tilde{\mathcal{H}}_{\text{GL}} \equiv \frac{\mathcal{H}_{\text{GL}}}{I_1}. \quad (8)$$

The resulting GL energy functional reads

$$\begin{aligned} \tilde{\mathcal{H}}_{\text{GL}} = \int d\mathbf{r} & \left\{ -\frac{1}{2} \left[(\partial_x \mathbf{S}_r)^2 + (\partial_y \mathbf{S}_r)^2 \right] + \frac{1}{2} \left(\partial_x^2 \mathbf{S}_r + \partial_y^2 \mathbf{S}_r \right)^2 \right. \\ & \left. + \frac{\tilde{\Gamma}}{2} \left[(\partial_x S_r^x)^2 + (\partial_y S_r^y)^2 \right] - \tilde{D} (S_r^z)^2 - \tilde{H} S_r^z \right\} \\ & - \frac{I_3}{I_2} \int d\mathbf{r} \left(\partial_x^2 \mathbf{S}_r \right) \cdot \left(\partial_y^2 \mathbf{S}_r \right). \end{aligned} \quad (9)$$

The $T = 0$ variational phase diagrams for the GL theory Eq. (9) with $\tilde{\Gamma} = \{0, 0.4, 0.8, 1.2\}$ and $I_3 = 0$ (see Fig. 4) are qualitatively similar to the ones obtained for the microscopic model (Fig. 1). This fact demonstrates the universal character of the newly discovered multi- \mathbf{Q} orderings. We can then use the GL functional Eq. (9) to understand the general principle behind the emergence of the MX and VtX phases.

The first observation is that the ordering wavevectors \mathbf{Q}_1 and \mathbf{Q}_2 of the double- \mathbf{Q} states remain parallel to the principal x and y directions even for $I_3 > 0$. The reason is that the \mathbf{q} -dependent part of the Γ -term favors proper screw spirals, $\mathbf{S}_r = (0, \cos(\mathbf{Q}_1 \cdot \mathbf{r}), \sin(\mathbf{Q}_1 \cdot \mathbf{r}))$ and $\mathbf{S}_r = (\cos(\mathbf{Q}_2 \cdot \mathbf{r}), 0, \sin(\mathbf{Q}_2 \cdot \mathbf{r}))$, that propagate along these directions. Indeed, these principal directions become energetically favorable for $I_3/I_2 < \tilde{\Gamma}(1 - \tilde{\Gamma}/8)$. This observation allows us to understand the stabilization mechanism of the double- \mathbf{Q} MX-II phase that is approximately described by the equation

$$m_r^x = \pm a_1 \sin(\mathbf{Q}_2 \cdot \mathbf{r}), \quad (10a)$$

$$m_r^y = \pm a_1 \sin(\mathbf{Q}_1 \cdot \mathbf{r}), \quad (10b)$$

$$m_r^z = a_0 + a_2 \cos(\mathbf{Q}_1 \cdot \mathbf{r}) \cos(\mathbf{Q}_2 \cdot \mathbf{r}), \quad (10c)$$

where $\mathbf{S}_r \equiv \mathbf{m}_r / |\mathbf{m}_r|$. As it is clear from the phase diagram, the competing zero field phases are the conical (cycloidal) and vertical (proper screw) spiral orderings. A simple evaluation of the energies of these competing phases, which does not include the small higher harmonic components, produces a rough estimate of the stability interval of the MX-II phase at zero field (see Appendix E for more details):

$$-\frac{1}{2} + \frac{5}{32}(2 - \tilde{\Gamma})^2 - \frac{I_3}{4I_2} \lesssim \tilde{D} \lesssim -\frac{1}{12} + \frac{I_3}{6I_2}. \quad (11)$$

Note that a positive quartic anisotropy $0 < I_3/I_2 < \tilde{\Gamma}(1 - \tilde{\Gamma}/8)$ lowers the exchange energy cost of the MX-II phase (the first harmonics of this phase are $\pm \mathbf{Q}_1 \pm \mathbf{Q}_2$). According to Eqs. (6) and (8), the \mathbf{q} -independent contribution of the Γ -term can turn the single-ion term into an effective easy-plane anisotropy $\tilde{D} < 0$. This explains the suppression of the VS phase in favor of the MX-II phase, which has stronger in-plane (XY) spin components. The MX-II phase is also more stable than the CS because of the \mathbf{q} -dependent contribution of the Γ term increases the energy cost of the CS phase by an amount proportional to $\tilde{\Gamma}Q^2$ (see Appendix E for more details).

For positive I_3 , the compass anisotropy $\tilde{\Gamma}$ must be strong enough to guarantee that the ordering wavevectors remain parallel to the principal x and y directions. These conditions can be naturally fulfilled by tetragonal metallic systems, such as $4f$ -electron materials, with dominant RKKY interactions and a small Fermi surface. The combination of a small Fermi surface and strong spin-orbit coupling can naturally lead to $0 < I_3/I_2 < \tilde{\Gamma}(1 - \tilde{\Gamma}/8)$.

IV. ANOMALOUS HALL EFFECT IN 2D

The net scalar spin chirality of the double- \mathbf{Q} states MX-I and MX-II creates an effective U(1) gauge flux [29] for itinerant electrons that are coupled via exchange to the magnetic moments \mathbf{S}_i . The resulting non-zero Berry curvature of the (reconstructed) electronic bands leads to anomalous Hall effect (AHE). Unlike typical realizations of field-induced SkX, the MX-I and MX-II states can be realized at zero field and

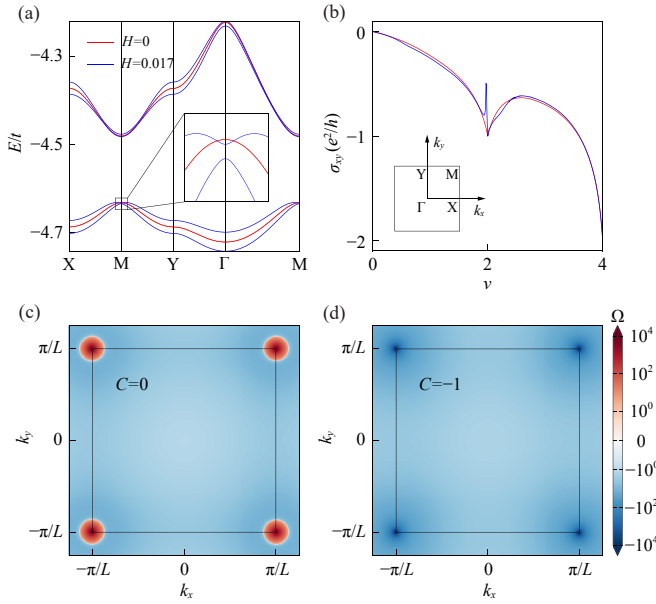


Figure 5. Reconstructed band dispersion, transverse conductivity, and Berry curvature of the lowest electronic bands due to coupling to the MX-II state. The MX-II states that we used here are obtained for $J_1 = -1$, $J_2 = 0.35$, $J_3 = 0.15$, $\Gamma = 0.3$, and $D = 0.16$ in the $L = 8$ variational space (Appendix A), and $J/t = 1$. (a) Lowest four reconstructed electronic bands due to coupling to $H = 0$ MX-II state (red solid curves, doubly degenerate) and MX-II state distorted by an in-plane field along [110] direction with $H = 0.017$ (blue solid curves). (b) Transverse conductivities as a function of filling for the four lowest bands in (a). Here the filling fraction $\nu = n$ indicates the lowest n bands are filled. The inset in (b) shows the first BZ of the magnetic superlattice. (c)(d) Berry curvatures of the two lowest bands in (a), obtained with the MX-II state distorted by an in-plane field along the [110] direction with $H = 0.017$. The black squares enclose the folded first BZ.

produce a spontaneous topological Hall effect⁴.

This simple phenomenon can be illustrated by coupling the local moments \mathbf{S}_i to the spins of itinerant electrons [16]:

$$\mathcal{H}_K = -t \sum_{\langle ij \rangle, \sigma} (c_{i\sigma}^\dagger c_{j\sigma} + h.c.) + J \sum_{i, \alpha\beta} c_{i\alpha}^\dagger \sigma_{\alpha\beta} c_{i\beta} \cdot \mathbf{S}_i, \quad (12)$$

where the first term is the nearest neighbor hopping, and the second term represents the exchange interaction J between the itinerant electrons and the local moments. By assuming that the effective spin-spin interaction mediated by the conduction electrons is much smaller than the relevant exchange energy scales in Eq. (1), we can still use the magnetic phase diagram obtained for \mathcal{H} (Fig. 1). As discussed below, the topological properties of the itinerant electrons are mainly dictated by symmetry, so the choice of nearest neighbor hopping in Eq. (12) is a matter of convenience.

⁴ In other centrosymmetric models, skyrmion crystals typically only exist for finite magnetic field and the degeneracy of the skyrmion crystal solutions with opposite chiralities can be lifted the orbital coupling to the external field [30].

For long period ($Q \ll 1$) incommensurate states, the (folded) first Brillouin zone (BZ) includes a large number of reconstructed electronic bands. **The transverse conductivity depends on the filling fraction. For the purpose of illustration, we will focus on the four lowest energy bands (our results can be easily generalized to include more bands).** Figure 5(a) shows the reconstructed electronic bands for the MX-II state, which turn out to be doubly degenerate at $H = 0$. This degeneracy is protected by the combined symmetries $O_1 = \mathcal{I}C_{2z}$ and $O_2 = \left\{ C_{2x} \overline{\mathcal{M}}_y | \frac{1}{2}, 0, 0 \right\}$ (Appendix F). A finite magnetic field along the z axis breaks O_2 and partially lifts the degeneracy except for the folded BZ boundaries, which are protected by the non-symmorphic symmetries $O_3 = \left\{ \mathcal{T} \mathcal{M}_y | \frac{1}{2}, 0, 0 \right\}$ and $O_4 = \left\{ \mathcal{T} \mathcal{M}_x | 0, \frac{1}{2}, 0 \right\}$ [31] (Appendix F). The remaining degeneracies can be fully lifted by applying an in-plane magnetic field along the [110] direction [Fig. 5(a)] that distorts the MX-II state.

The MX-II state produces anomalous Hall conductivity even in absence of magnetic field, implying that the Hall effect is purely of topological origin. As shown in Fig. 5(b), a value as large as $|\sigma_{xy}| = 2e^2/h$ can be achieved by completely filling the four lowest bands. Figures 5(c)(d) show the Berry curvatures of the two lowest bands depicted in Fig. 5(a). The direct field-induced gap between these two bands reaches the minimum value at the M point of the folded BZ [see inset of Fig. 5(a)] producing a sharp increase of the Berry curvature [Figs. 5(c)(d)] and a sharp peak of σ_{xy} around band filling $\nu = 2$ [Fig. 5(b)]⁵. The resulting Chern number of the lower (higher) energy band is $C = 0$ (-1). Although the Berry curvature of the lowest band is large and positive at the M point, it is negative and small in the rest of the BZ [Fig. 5(c)], leading to a cancellation of the Chern number. Consequently, the Hall conductivity becomes quantized at $\sigma_{xy} = -e^2/h$ for filling fraction $\nu = 2$. Similarly, $\sigma_{xy} = 2e^2/h$ for filling fraction $\nu = 4$ because the total Chern number of the four lowest bands is $C = -2$ [see Fig. 5(b)]. Note that the signs of C and σ_{xy} are controlled by the sign of scalar chirality of the MX-II state, which can be flipped without energy cost.

V. MAGNETIC WEYL SEMIMETAL IN 3D

Weyl semimetals are realized in crystals with broken time-reversal or inversion symmetry [32]. In particular, it was proposed that topological spin textures and Weyl points could affect each other in the same material [33]. As we demonstrate below, Weyl points can be systematically generated by coupling the conduction electrons to vertically stacked layers of MX-II states. The $O_{n=1,2,3,4}$ symmetries of 2D MX-II state can be generalized to 3D MX-II state as $O_n \overline{\mathcal{M}}_z$ (Appendix F). In the $H = 0$ case, all the bands are doubly degenerate in the whole BZ, and the degeneracy is protected by the combined symmetries $O_1 \overline{\mathcal{M}}_z$ and $O_2 \overline{\mathcal{M}}_z$ (Appendix F).

⁵ Here the filling $\nu = n$ indicates that the lowest n bands are filled.

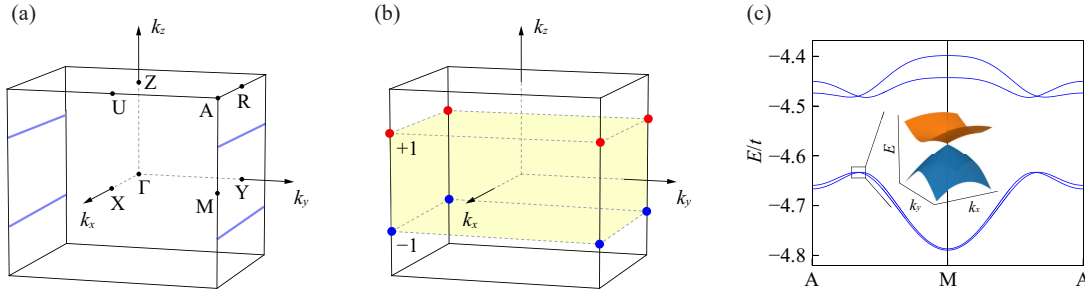


Figure 6. Nodal lines and Weyl points generated by coupling vertically stacked MX-II states to itinerant electrons. The MX-II states used in this calculation were obtained with $J_1 = -1$, $J_2 = 0.35$, $J_3 = 0.15$, $\Gamma = 0.3$, and $D = 0.16$ in the $L = 8$ variational space (Appendix A). (a) Nodal lines at $\mathbf{k} = (k_x, \pi/L, \pm\pi/2)$ are generated by distorting the MX-II state with an in-plane field H_y along the [010] direction, and a finite SOC in the interlayer hopping t_z . (b) Weyl points marked by red and blue spots with topological charges ± 1 , respectively, are generated by further adding intralayer hopping t_x with finite SOC. (c) Electronic dispersion of the four lowest bands along A \rightarrow M \rightarrow A direction, where the inset shows a zoomed-in view near the Weyl points. The parameters used in (c) are $J = t$, $H_y = 0.012t$, $t_z = 0.1t$, and $t_x = 0.05t$.

Weyl points can be generated by partially lifting this double degeneracy, which can be done in different ways. For instance, the distortion of the spin texture induced by an in-plane field H_y along the [010] direction breaks the $O_1\overline{M}_z$, $O_2\overline{M}_z$, and $O_3\overline{M}_z$ symmetries, leaving a nodal surface at the BZ side $\mathbf{k} = (k_x, \pi/L, k_z)$ protected by $O_4\overline{M}_z$, where L is the lattice constant of the magnetic superlattice. Further inclusion of the spin-orbit coupling (SOC) in the interlayer hopping $t_z \sum_i \sum_{\alpha\beta} (c_{i+\hat{z},\alpha}^\dagger \sigma_{\alpha\beta}^x c_{i\beta} + h.c.)$ gaps out the nodal surfaces except for two nodal lines at $\mathbf{k} = (k_x, \pi/L, \pm\pi/2)$, where the distance between two nearest neighbor MX-II layers is set as unity [Fig. 6(a)]. The SOC-induced conversion of the nodal surface into two nodal lines can be easily understood by noticing that the Fourier transform of the SOC term vanishes at $k_z = \pm\pi/2$ (Appendix F).

Finally, a further inclusion of SOC in the intralayer hopping, $t_x \sum_i \sum_{\alpha\beta} (c_{i+\hat{x},\alpha}^\dagger \sigma_{\alpha\beta}^x c_{i\beta} + h.c.)$, lifts the degeneracy of the nodal lines and generates pairs of Weyl points with opposite chirality in the folded first BZ [Figs. 6(b)(c)]. The chirality of a Weyl point is characterized by the topological charge that counts the total Berry curvature flux emitted or absorbed by the Weyl point [34]. In our system, each pair of vertically aligned Weyl points carry opposite topological charges $C = \pm 1$ [Fig. 6(b)]. Then 2D energy bands for fixed k_z values between the two Weyl points [highlighted in Fig. 6(b)] carry a nonzero Chern number. Thus, the contribution of each pair of Weyl points to the quantum anomalous Hall effect (σ_{xy}) increases with their separation, which can be tuned by changing the ratio t_x/t_z [35].

VI. SUMMARY AND DISCUSSION

Our work introduces a new guiding principle for the stabilization of novel topological spin textures in centrosymmetric tetragonal magnets. The magnetic unit cell of these crystals comprises four merons, whose net skyrmion charge can be ± 2 (MX-II), ± 1 (MX-I) and 0 (VtX). The three phases are double-

Q orderings obtained from the superposition of two proper screw (vertical) spirals that propagate along perpendicular directions with a wavenumber Q dictated by competing exchange interactions (magnetic frustration). The key observation is that the above-mentioned double- Q vertical spiral orderings result from the competition between easy-axis and compass anisotropies. The combination of these two terms can produce a relatively weak *effective easy-plane* anisotropy $\tilde{D} < 0$ and a rather strong q -dependent component of the compass anisotropy $\tilde{\Gamma}$, that penalizes the conical phase. An effective easy-plane single-ion anisotropy favors the double- Q vertical spiral orderings relative to the single- Q vertical spiral phase because, on average, the MXs and the VtX have a stronger in-plane component of the spins than the VS.

It is important to note that these double- Q phases could be further stabilized by effective four-spin interactions that are naturally generated in systems where the interaction between local moments is mediated by conduction electrons [22, 36, 37]. In this case, the compass anisotropy alone (without the need of a bare single-ion anisotropy) should be enough to stabilize the MX-I, MX-II and VtX phases. Since these conditions can be naturally fulfilled by f -electron magnets, our results indicate that tetragonal f -electron materials with relatively weak single-ion anisotropy are natural candidates to host these phases. This hypothesis is supported by the recent experimental results in the centrosymmetric tetragonal material GdRu₂Si₂ [15].

While we have focused on the $T = 0$ limit, all of the reported phases break discrete symmetries, which should not be immediately restored by thermal fluctuations. The finite temperature phase diagram and its dependence on dimensionality are left for future studies based on Monte-Carlo simulations [18].

Finally, the effective U(1) gauge flux [29] generated by the MXs produces anomalous Hall effect in metallic systems even at zero field. Moreover, a symmetry analysis reveals that the reconstructed electronic bands can naturally include Weyl points for 3D versions of the MX phases, that lead to a magnetic Weyl semimetal for certain filling fractions.

ACKNOWLEDGMENTS

Z.W. and C.D.B. were supported by funding from the Lincoln Chair of Excellence in Physics. During the writing of this manuscript, Z.W. was supported by the U.S. Department of Energy through the University of Minnesota Center for Quantum Materials, under Award No. DE-SC-0016371. The work at Los Alamos National Laboratory (LANL) was carried out under the auspices of the U.S. DOE NNSA under Contract No. 89233218CNA000001 through the LDRD Program, and was supported by the Center for Nonlinear Studies at LANL. This research used resources of the Oak Ridge Leadership Computing Facility at the Oak Ridge National Laboratory, which is supported by the Office of Science of the U.S. Department of Energy under Contract No. DE-AC05-00OR22725.

Appendix A: Variational Methods

The variational methods used in this paper follow closely ref. [24] except for some fine details.

We start by assuming that the ground state magnetic supercell contains $L \times L$ spins spanned by the basis $\{L\mathbf{a}_1, L\mathbf{a}_2\}$, where \mathbf{a}_1 and \mathbf{a}_2 are the basis of the square lattice. In other words, the ground state ordering wavenumber Q is fixed by $Q = l|\mathbf{b}_1|/L$, where l is another integer satisfying $l < L$. We first try several integer values of L which is given by

$$L \approx 2\pi/Q_0, \quad 2\pi/Q_0 \pm 1, \quad 2\pi/Q_0 \pm 2, \dots, \quad (\text{A1})$$

where Q_0 is the wavenumber that minimizes Eq. (2). Clearly, if the true ground state is incommensurate to the choices of L (typically ranges from 4 to 10 for the parameters considered in this work), a systematic error is introduced in the energy calculation. To resolve this issue, we will relax this variational constraint later.

The spin states are described by $2 \times L \times L$ variational parameters $\{\theta_r, \phi_r\}$ that parametrize the spin space with $|\mathcal{S}_r| = 1$. The total energy density of Eq. (1) is then numerically minimized in this variational space [38]. Finally, for any given parameter set $\{J_1, J_2, J_3, \Gamma, D, H\}$, we pick the lowest energy solution among the different choices of L .

Such a variational calculation is unbiased, in the sense that we are not making any assumption of the spin structure, except for the size of the underlying magnetic unit cell. However, the phase boundaries will not be very accurate since the ordering wavenumber Q is generally incommensurate. To further improve the phase boundaries, we will perform another calculation where Q is included as a variational parameter.

To prepare for the refined variational calculation, we first perform a Fourier analysis of the phases discovered by the ‘‘unbiased’’ variational method and parametrize them by a few dominant Fourier components (Appendix D). With such parametrization, we can relax the magnetic supercell assumption, and include the ordering wavenumber as a variational parameter. For each point in the phase diagrams, we compare the optimized energies of different ansatze and pick the lowest one.

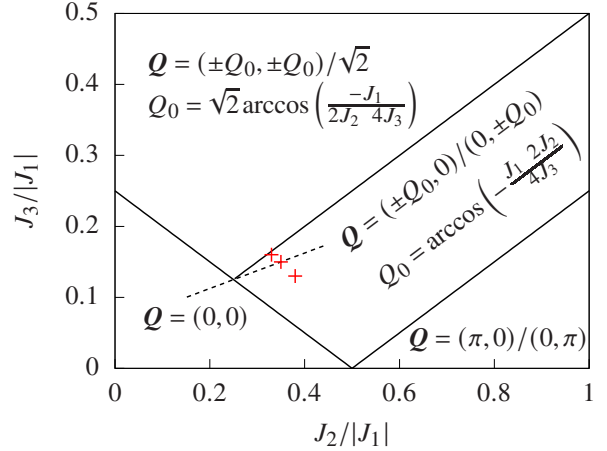


Figure 7. Phase diagram showing the positions of the ordering wavevectors for the square lattice Heisenberg model with $J_1 < 0$ (FM) at $T = 0$. The symbols correspond to the values of $\{J_1, J_2, J_3\}$ used in Fig. 1 in the main text. The dashed line corresponds to $J_3 = 0$.

The energy minimization of different ansatze are performed on a finite 512×512 square lattice for the microscopic model [38]. For the GL theory, we obtain the $T = 0$ phase diagrams by discretizing the real space continuum and replacing derivatives by finite difference. Then, we optimize different variational ansatze and find the lowest energy solution. The linear dimension of the real space continuum is set to 200, and we typically discretize it by a 200×200 mesh. Note that the phase boundary between $\text{VS}'(\Delta)$ and VS states [Fig. 4(a)] requires a mesh as fine as 1600×1600 for a good convergence.

Appendix B: Ordering wavevectors of the Heisenberg exchanges

The ordering wavevectors of the square lattice Heisenberg model (no anisotropy or magnetic field) can be determined by minimizing the exchange interaction Eq. (2). The results for $J_1 < 0$ (FM) are presented in Fig. 7. Note that this analysis is no longer valid in the presence of magnetic field (Zeeman) and spin anisotropies because lowest energy state is not necessarily a single- Q spiral ordering. Consequently, Q must be treated as an additional variational parameter to determine the lowest energy state (Appendix A).

Depending on the sign of $2J_3 - J_2$, the incommensurate ordering wavevectors are located on different principle axes (Fig. 7):

- For $2J_3 < J_2$, $Q = (\pm Q_0, 0)$ or $(0, \pm Q_0)$, where $Q_0 = \arccos\left(-\frac{J_1+2J_2}{4J_3}\right)$;
- For $2J_3 > J_2$, $Q = (\pm Q_0, \pm Q_0)/\sqrt{2}$, where $Q_0 = \sqrt{2} \arccos\left(\frac{-J_1}{2J_2+4J_3}\right)$.

In Fig. 1 in the main text, we take three points in the region with $Q = (\pm Q_0, 0)/(0, \pm Q_0)$, all of which gives roughly $Q_0 \approx \frac{2\pi}{6}$ (see Fig. 7).

In the long wavelength limit, we can expand Eq. (2):

$$J(\mathbf{q}) \approx I_0 - \frac{I_1}{2} q^2 + \frac{I_2}{2} q^4 - I_3 q_x^2 q_y^2, \quad (\text{B1})$$

with $I_0 = 2(J_1 + J_2 + J_3)$ and

$$I_1 = J_1 + 2J_2 + 4J_3, \quad I_2 = \frac{J_1 + 2J_2 + 16J_3}{12}, \quad I_3 = I_2 - \frac{J_2}{2}. \quad (\text{B2})$$

In this limit, the direction of the ordering wavevector \mathbf{Q} is determined by the sign of the quartic anisotropy I_3 (see dashed line in Fig. 7):

- For $I_3 < 0$, $\mathbf{Q} = (\pm Q_0, 0)$ or $(0, \pm Q_0)$, where $Q_0 = \sqrt{I_1/2I_2}$;
- For $I_3 > 0$, $\mathbf{Q} = (\pm Q_0, \pm Q_0)/\sqrt{2}$, where $Q_0 = \sqrt{I_1/(2I_2 - I_3)}$.

Appendix C: Skyrmion charge of MX-I, MX-II, and VtX states

The skyrmion charge is defined by

$$n_{\text{sk}} = \frac{1}{4\pi} \int d\mathbf{r} \mathbf{S}_r \cdot (\partial_x \mathbf{S}_r \times \partial_y \mathbf{S}_r), \quad (\text{C1})$$

which corresponds to the area spanned by the unit vector field \mathbf{S}_r (in units of the area 4π of the unit sphere) when the two dimensional real space $\mathbb{R}^2 \cup \{\infty\}$ is mapped to S^2 via stereographic projection. A single skyrmion “wraps” the sphere only once and yields $n_{\text{sk}} = \pm 1$ (the sign is defined by the sign of scalar chirality). A meron corresponds to a half covering, which yields $n_{\text{sk}} = \pm 1/2$, while the skyrmion charge of a vortex is generally an arbitrary number different from 1 or $1/2$.

Figure 8 shows the vector-contour plots of the MX-II, MX-I, and VtX states. It is clear that the MX-II state contains four merons in each magnetic unit cell. The skyrmion charge for a magnetic unit cell can be read out directly from Fig. 8(a): $n_{\text{sk}} = -\frac{1}{2} \times 4 = -2$. Note that the other choice of $n_{\text{sk}} = 2$ has the same energy for the model Eq. 1 considered in the main text, which can be obtained by simply changing the sign of S_r^y at every site. The MX-I state contains four vortices (or equivalently, four overlapping merons) in each magnetic unit cell [Fig. 8(b)]. Denote the skyrmion charge of the largest

vortex ($S_r^z < 0$ in the center) as α ($1/2 < \alpha < 1$), then the two vortices centered at the elliptical contours have skyrmion charge roughly $1 - \alpha$ each, and the last vortex has skyrmion charge $-(1 - \alpha)$. Thus, the net skyrmion charge of MX-I is $n_{\text{sk}} = \alpha + 2 \times (1 - \alpha) - (1 - \alpha) = 1$. Same as the MX-II case, the $n_{\text{sk}} = \pm 1$ solutions have the same energy in MX-I. The VtX state has four vortices in the magnetic unit cell, whose skyrmion charges cancel out with each other, giving $n_{\text{sk}} = 0$ [Fig. 8(c)].

Appendix D: Fourier analysis of different states

The states that appear in this paper can be parametrized by a few dominant Fourier components. We first focus on the single- \mathbf{Q} and double- \mathbf{Q} states, which involve at most two perpendicular wavevectors

$$\mathbf{Q}_1 = (Q, 0), \quad \mathbf{Q}_2 = (0, Q), \quad (\text{D1})$$

and $0 < Q < \pi$.

The normalized spin configurations $\mathbf{S}_r \equiv \mathbf{m}_r/|\mathbf{m}_r|$ of the VS and VS' states can be parametrized by

$$m_{r-r_0}^x = a_1 \sin(\mathbf{Q}_2 \cdot \mathbf{r}) + a_2 \sin(2\mathbf{Q}_2 \cdot \mathbf{r}) + a_3 \sin(3\mathbf{Q}_2 \cdot \mathbf{r}), \quad (\text{D2a})$$

$$m_{r-r_0}^y = a_4 \sin(\mathbf{Q}_1 \cdot \mathbf{r}), \quad (\text{D2b})$$

$$m_{r-r_0}^z = a_0 + a_5 \cos(\mathbf{Q}_2 \cdot \mathbf{r}) + a_6 \cos(2\mathbf{Q}_2 \cdot \mathbf{r}) + a_7 \cos(3\mathbf{Q}_2 \cdot \mathbf{r}). \quad (\text{D2c})$$

The difference between the VS and VS' states is that $a_4 = 0$ in the VS while it is nonzero in the VS'.

The normalized spin configurations $\mathbf{S}_r \equiv \mathbf{m}_r/|\mathbf{m}_r|$ of the CS state can be parametrized by

$$m_{r-r_0}^x = a_1 \cos(\mathbf{Q}_1 \cdot \mathbf{r}) + a_2 \cos(3\mathbf{Q}_1 \cdot \mathbf{r}), \quad (\text{D3a})$$

$$m_{r-r_0}^y = a_3 \sin(\mathbf{Q}_1 \cdot \mathbf{r}) + a_4 \sin(3\mathbf{Q}_1 \cdot \mathbf{r}), \quad (\text{D3b})$$

$$m_{r-r_0}^z = a_0 + a_5 \cos(2\mathbf{Q}_1 \cdot \mathbf{r}). \quad (\text{D3c})$$

The normalized spin configurations $\mathbf{S}_r \equiv \mathbf{m}_r/|\mathbf{m}_r|$ of the MX-I, MX-II, and VtX states can be universally parametrized by

$$m_{r-r_0}^x = \pm \sin(\mathbf{Q}_2 \cdot \mathbf{r}) [a_1 + a_2 \cos(\mathbf{Q}_1 \cdot \mathbf{r}) + a_3 \cos(\mathbf{Q}_2 \cdot \mathbf{r}) + a_4 \cos(2\mathbf{Q}_1 \cdot \mathbf{r}) + a_9 (1 + 2 \cos(2\mathbf{Q}_2 \cdot \mathbf{r}))], \quad (\text{D4a})$$

$$m_{r-r_0}^y = \pm \sin(\mathbf{Q}_1 \cdot \mathbf{r}) [a_1 + a_2 \cos(\mathbf{Q}_2 \cdot \mathbf{r}) + a_3 \cos(\mathbf{Q}_1 \cdot \mathbf{r}) + a_4 \cos(2\mathbf{Q}_2 \cdot \mathbf{r}) + a_9 (1 + 2 \cos(2\mathbf{Q}_1 \cdot \mathbf{r}))], \quad (\text{D4b})$$

$$m_{r-r_0}^z = a_0 + a_5 [\cos(\mathbf{Q}_1 \cdot \mathbf{r}) + \cos(\mathbf{Q}_2 \cdot \mathbf{r})] + a_6 [\cos(2\mathbf{Q}_1 \cdot \mathbf{r}) + \cos(2\mathbf{Q}_2 \cdot \mathbf{r})] + a_7 \cos(\mathbf{Q}_1 \cdot \mathbf{r}) \cos(\mathbf{Q}_2 \cdot \mathbf{r}) + a_8 [\cos(2\mathbf{Q}_1 \cdot \mathbf{r}) \cos(\mathbf{Q}_2 \cdot \mathbf{r}) + \cos(2\mathbf{Q}_2 \cdot \mathbf{r}) \cos(\mathbf{Q}_1 \cdot \mathbf{r})], \quad (\text{D4c})$$

where the \pm choice controls the sign of the skyrmion charge

of each meron and vortex.

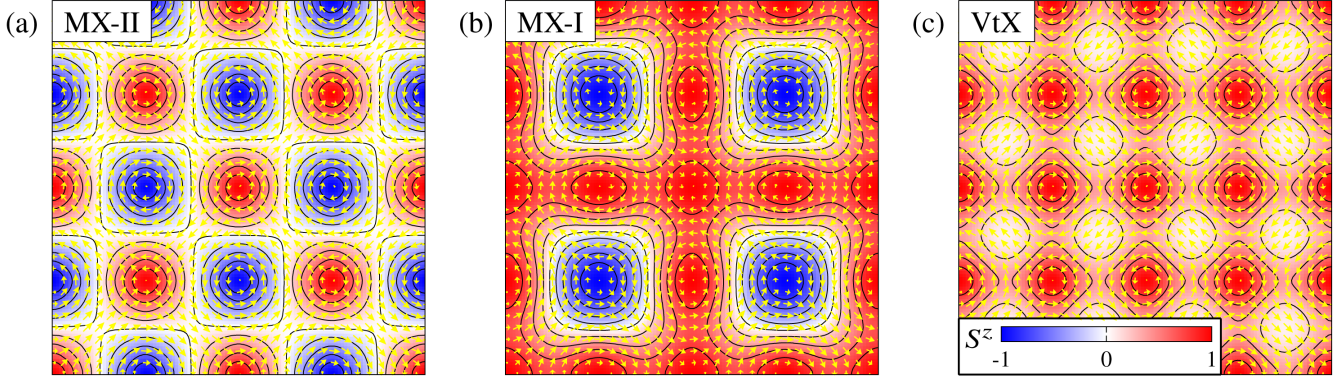


Figure 8. Vector-contour plots of the MX-II, MX-I, and VtX states with the parametrization given in Eq. (D4). The arrows represent the xy components of the spins, and the background colors represent the z component of the spins. The contours are taken at linear incremental level with $\Delta S^z = 0.2$. (a) The parameters used in MX-II are $a_0 = 0.025$, $a_1 = 1$, $a_4 = 0.016$, $a_7 = 0.689$, $a_9 = 0.056$, and $a_2 = a_3 = a_5 = a_6 = a_8 = 0$. (b) The parameters used in MX-I are $a_0 = 0.288$, $a_1 = 1$, $a_2 = -0.345$, $a_3 = -0.173$, $a_4 = 0.067$, $a_5 = 0.48$, $a_6 = 0.044$, $a_7 = -0.762$, $a_8 = 0.081$, and $a_9 = 0.024$. (c) The parameters used in VtX are $a_0 = 0.395$, $a_1 = 1$, $a_4 = -0.011$, $a_6 = 0.162$, $a_9 = 0.03$, and $a_2 = a_3 = a_5 = a_7 = a_8 = 0$.

We continue with the parametrization of the triple- \mathbf{Q} states, which are known to exist in the long wavelength limit from the GL theory [20]. Note that these states are not favored by the spatial anisotropy of the square lattice.

The ordering wavevectors $\{\mathbf{Q}_1, \mathbf{Q}_2, \mathbf{Q}_3\}$ are parametrized by a single parameter in the continuum limit because $|\mathbf{Q}_1| = |\mathbf{Q}_2| = |\mathbf{Q}_3|$ and their directions differ by $\pm 120^\circ$ rotations. The following parametrization

$$\begin{aligned} \mathbf{Q}_1 &= (Q_a \cos \alpha, -Q_a \sin \alpha), \\ \mathbf{Q}_2 &= (0, Q_b), \\ \mathbf{Q}_3 &= -(Q_a \cos \alpha, Q_a \sin \alpha), \end{aligned} \quad (\text{D5})$$

includes the three ordering wavevectors in the continuum limit of the theory (very weak lattice anisotropy) as well as the corrections by the square lattice anisotropy. The optimal values from the minimization are found to be $Q_a \approx Q_b$ and $\alpha \approx \frac{\pi}{6}$ on a finite square lattice (the approximated relations become exact in the thermodynamic limit). Then, the parametrization of the triple- \mathbf{Q} states follow the ones in Refs. [19, 20, 24].

The normalized spin configurations $\mathbf{S}_r \equiv \mathbf{m}_r / |\mathbf{m}_r|$ of the

$\text{VS}'(\Delta)$ state can be parametrized as

$$m_{r-r_0}^x = a_1 \cos \phi \sin(\mathbf{Q}_2 \cdot \mathbf{r}) + a_2 \sin \phi [\cos(\mathbf{Q}_1 \cdot \mathbf{r}) + \cos(\mathbf{Q}_3 \cdot \mathbf{r})], \quad (\text{D6a})$$

$$m_{r-r_0}^y = a_1 \sin \phi \sin(\mathbf{Q}_2 \cdot \mathbf{r}) - a_2 \cos \phi [\cos(\mathbf{Q}_1 \cdot \mathbf{r}) + \cos(\mathbf{Q}_3 \cdot \mathbf{r})], \quad (\text{D6b})$$

$$m_{r-r_0}^z = a_0 - a_1 \cos(\mathbf{Q}_2 \cdot \mathbf{r}). \quad (\text{D6c})$$

The normalized spin configurations $\mathbf{S}_r \equiv \mathbf{m}_r / |\mathbf{m}_r|$ of the $2\mathbf{Q}$ -CS(Δ) and $2\mathbf{Q}$ -CS'(Δ) states can be parametrized as

$$m_{r-r_0}^x = a_1 \sin(\mathbf{Q}_1 \cdot \mathbf{r}) + a_2 \sin(\mathbf{Q}_3 \cdot \mathbf{r}), \quad (\text{D7a})$$

$$m_{r-r_0}^y = a_1 \cos(\mathbf{Q}_1 \cdot \mathbf{r}) - a_2 \cos(\mathbf{Q}_3 \cdot \mathbf{r}), \quad (\text{D7b})$$

$$m_{r-r_0}^z = a_0 + a_3 \cos(\mathbf{Q}_2 \cdot \mathbf{r}), \quad (\text{D7c})$$

where $a_1 = a_2$ in the $2\mathbf{Q}$ -CS(Δ) state, while $a_1 \neq a_2$ in the $2\mathbf{Q}$ -CS'(Δ) state.

The normalized spin configurations $\mathbf{S}_r \equiv \mathbf{m}_r / |\mathbf{m}_r|$ of the SkX(Δ) state can be parametrized as

$$m_{r-r_0}^x = a_1 \left[\cos(\varphi) \sin(\mathbf{Q}_1 \cdot \mathbf{r}) + \cos\left(\varphi + \kappa \frac{2\pi}{3}\right) \sin(\mathbf{Q}_2 \cdot \mathbf{r}) + \cos\left(\varphi + \kappa \frac{4\pi}{3}\right) \sin(\mathbf{Q}_3 \cdot \mathbf{r}) \right], \quad (\text{D8a})$$

$$m_{r-r_0}^y = a_1 \left[\sin(\varphi) \sin(\mathbf{Q}_1 \cdot \mathbf{r}) + \sin\left(\varphi + \kappa \frac{2\pi}{3}\right) \sin(\mathbf{Q}_2 \cdot \mathbf{r}) + \sin\left(\varphi + \kappa \frac{4\pi}{3}\right) \sin(\mathbf{Q}_3 \cdot \mathbf{r}) \right], \quad (\text{D8b})$$

$$m_{r-r_0}^z = a_0 - a_2 [\cos(\mathbf{Q}_1 \cdot \mathbf{r}) + \cos(\mathbf{Q}_2 \cdot \mathbf{r}) + \cos(\mathbf{Q}_3 \cdot \mathbf{r})], \quad (\text{D8c})$$

where $\kappa = \pm 1$ controls the sign of the skyrmion charge, and φ controls the helicity. For simplicity, we have neglected the phases $\{\theta_1, \theta_2\}$ in Ref. [24], which are negligible when $|\mathbf{Q}_v| \ll 1$.

Appendix E: Stability estimate of the MX-II phase

To understand the stabilization mechanism of the MX-II phase at zero field, it is helpful to obtain rough estimates of

the energies of the CS, MX-II and VS states. Here, we work in the long wavelength limit with the rescaled GL functional.

The CS state at zero field can be approximated by

$$\mathbf{S}_r = (\cos(\mathbf{Q}_1 \cdot \mathbf{r}), \sin(\mathbf{Q}_1 \cdot \mathbf{r}), 0), \quad (\text{E1})$$

whose energy density is

$$e_{\text{CS}} = -\frac{Q^2}{2} + \frac{Q^4}{2} + \frac{\tilde{\Gamma}}{4}Q^2 = -\frac{(2-\tilde{\Gamma})^2}{32}, \quad (\text{E2})$$

where the optimal $Q = \frac{\sqrt{2-\tilde{\Gamma}}}{2}$.

The VS state at zero field can be approximated by

$$\mathbf{S}_r = (\sin(\mathbf{Q}_2 \cdot \mathbf{r}), 0, \cos(\mathbf{Q}_2 \cdot \mathbf{r})), \quad (\text{E3})$$

whose energy density is

$$e_{\text{VS}} = -\frac{Q^2}{2} + \frac{Q^4}{2} - \frac{\tilde{D}}{2} = -\frac{1}{8} - \frac{\tilde{D}}{2}, \quad (\text{E4})$$

where the optimal $Q = \frac{1}{\sqrt{2}}$.

The MX-II state at zero field is approximated by

$$m_r^x = \pm a_1 \sin(\mathbf{Q}_2 \cdot \mathbf{r}), \quad (\text{E5a})$$

$$m_r^y = \pm a_1 \sin(\mathbf{Q}_1 \cdot \mathbf{r}), \quad (\text{E5b})$$

$$m_r^z = a_2 \cos(\mathbf{Q}_1 \cdot \mathbf{r}) \cos(\mathbf{Q}_2 \cdot \mathbf{r}), \quad (\text{E5c})$$

where $\mathbf{S}_r = \mathbf{m}_r / |\mathbf{m}_r|$.

For $a_1 = a_2$, we obtain

$$S_q^x = \pm \sqrt{\frac{4}{5}} \pi \frac{\delta(\mathbf{q} + \mathbf{Q}_2) - \delta(\mathbf{q} - \mathbf{Q}_2)}{i}, \quad (\text{E6a})$$

$$S_q^y = \pm \sqrt{\frac{4}{5}} \pi \frac{\delta(\mathbf{q} + \mathbf{Q}_1) - \delta(\mathbf{q} - \mathbf{Q}_1)}{i}, \quad (\text{E6b})$$

$$S_q^z = \sqrt{\frac{1}{5}} \pi \left[\delta(\mathbf{q} + \mathbf{Q}_1 + \mathbf{Q}_2) + \delta(\mathbf{q} - \mathbf{Q}_1 - \mathbf{Q}_2) + \delta(\mathbf{q} + \mathbf{Q}_1 - \mathbf{Q}_2) + \delta(\mathbf{q} - \mathbf{Q}_1 + \mathbf{Q}_2) \right], \quad (\text{E6c})$$

after applying the sum rule in momentum space (note that we are neglecting higher harmonics). The energy density of this state is

$$e_{\text{MX-II}} = -\frac{3}{5}Q^2 + \frac{2}{5} \left(2 - \frac{I_3}{2I_2} \right) Q^4 - \frac{1}{5} \tilde{D} = -\frac{1}{10} - \frac{I_3}{20I_2} - \frac{1}{5} \tilde{D}, \quad (\text{E7})$$

where we have fixed $Q = \frac{1}{\sqrt{2}}$.

A comparison of the energies leads to an estimate of the stability condition for the MX-II state at zero field

$$-\frac{1}{2} + \frac{5}{32}(2-\tilde{\Gamma})^2 - \frac{I_3}{4I_2} \lesssim \tilde{D} \lesssim -\frac{1}{12} + \frac{I_3}{6I_2}. \quad (\text{E8})$$

Appendix F: Symmetry analysis of band degeneracy

In this section, we analyze the symmetries of the MX-II state which put restrictions on the electronic band structures of Eq. 12 in the main text.

The zero-field MX-II state has four important symmetries:

1. $O_1 = \mathcal{I}C_{2z}$;
2. $O_2 = \left\{ C_{2x} \overline{\mathcal{M}}_y | \frac{1}{2}, 0, 0 \right\}$;
3. $O_3 = \left\{ \mathcal{T} \mathcal{M}_y | \frac{1}{2}, 0, 0 \right\}$;
4. $O_4 = \left\{ \mathcal{T} \mathcal{M}_x | 0, \frac{1}{2}, 0 \right\}$.

Here O_2 , O_3 , and O_4 are nonsymmorphic symmetries with a glide reflection operation. $\overline{\mathcal{M}}_y$ is the space reflection operator under which $y \rightarrow -y$, while \mathcal{M}_y is the reflection operator acting on both space coordinate and spin as $y \rightarrow -y$, $S^x \rightarrow -S^x$, and $S^z \rightarrow -S^z$. \mathcal{I} is the inversion operator and \mathcal{T} is the time-reversal operator. C_{2x} and C_{2z} are two-fold rotation operators with the rotation axis along the x and z directions, respectively. $\left\{ \frac{1}{2}, 0, 0 \right\}$ represents a translation along the x direction by half a lattice constant of the magnetic superlattice.

As shown in the main text, the MX-II state is stable even in the absence of magnetic field. The four symmetries are present at zero field, resulting in double degeneracy of the electronic bands over the full Brillouin zone (BZ) [see Fig. 9(a)]. To prove this point, consider the symmetries O_1 and O_2 . Because $O_1^2 = -1$ and $[O_1, H(\mathbf{k})] = 0$, we can label the Bloch eigenfunctions of the Hamiltonian given in Eq. 12 by the eigenvalues $\pm i$ of the O_1 :

$$H(\mathbf{k})|\psi_{\pm}(\mathbf{k})\rangle = E_{\pm}(\mathbf{k})|\psi_{\pm}(\mathbf{k})\rangle, \quad (\text{F1})$$

and

$$O_1|\psi_{\pm}(\mathbf{k})\rangle = \pm i|\psi_{\pm}(\mathbf{k})\rangle. \quad (\text{F2})$$

Meanwhile, $[O_2, H(\mathbf{k})] = 0$ gives

$$H(\mathbf{k})O_2|\psi_{\pm}(\mathbf{k})\rangle = E_{\pm}(\mathbf{k})O_2|\psi_{\pm}(\mathbf{k})\rangle. \quad (\text{F3})$$

We then have two sets of eigenstates $|\psi_{\pm}(\mathbf{k})\rangle$ and $O_2|\psi_{\pm}(\mathbf{k})\rangle$ that have the same eigenvalues $E_{\pm}(\mathbf{k})$. Furthermore, since O_1 and O_2 anticommute, $\{O_1, O_2\} = 0$, we have

$$O_1 O_2 |\psi_{\pm}(\mathbf{k})\rangle = -O_2 O_1 |\psi_{\pm}(\mathbf{k})\rangle = \mp i O_2 |\psi_{\pm}(\mathbf{k})\rangle. \quad (\text{F4})$$

Therefore, $O_2|\psi_{\pm}(\mathbf{k})\rangle$ is also the eigenstate of O_1 with eigenvalue $\mp i$ that is opposite to that of $|\psi_{\pm}(\mathbf{k})\rangle$. Namely, $|\psi_{\pm}(\mathbf{k})\rangle$ and $O_2|\psi_{\pm}(\mathbf{k})\rangle$ are orthogonal states, implying that the energy bands are doubly degenerate. This combined symmetry can be broken by a net magnetization induced by an external magnetic field.

For the MX-II state that is obtained in the presence of a finite magnetic field along the z axis, the combined symmetry of O_1 and O_2 is broken. Consequently, the double degeneracy is no longer present in the whole BZ. However, it is still present along the boundary of the folded first BZ, which is protected by the symmetries O_3 and O_4 .

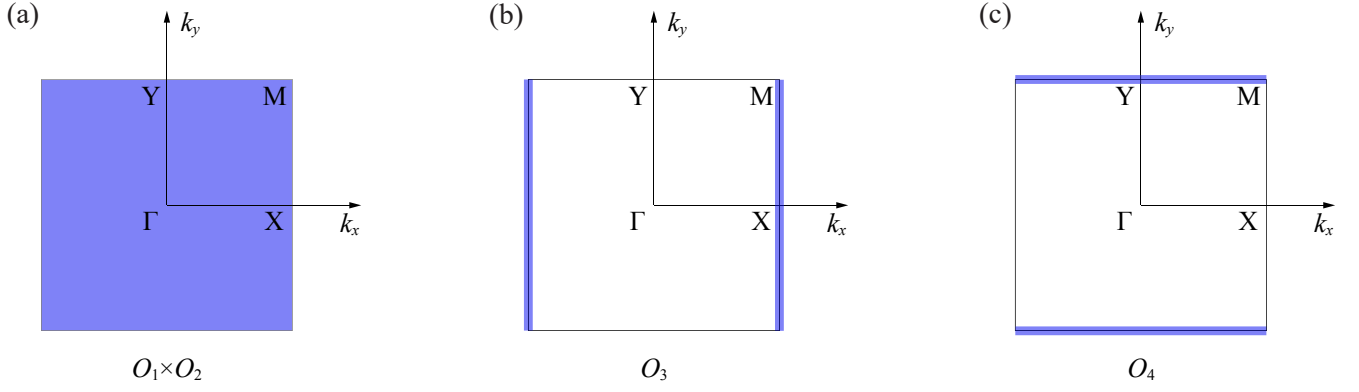


Figure 9. Double degeneracy of the electronic bands coupled to 2D MX-II state. Blue shades mark the double degeneracy protected by the corresponding symmetries.

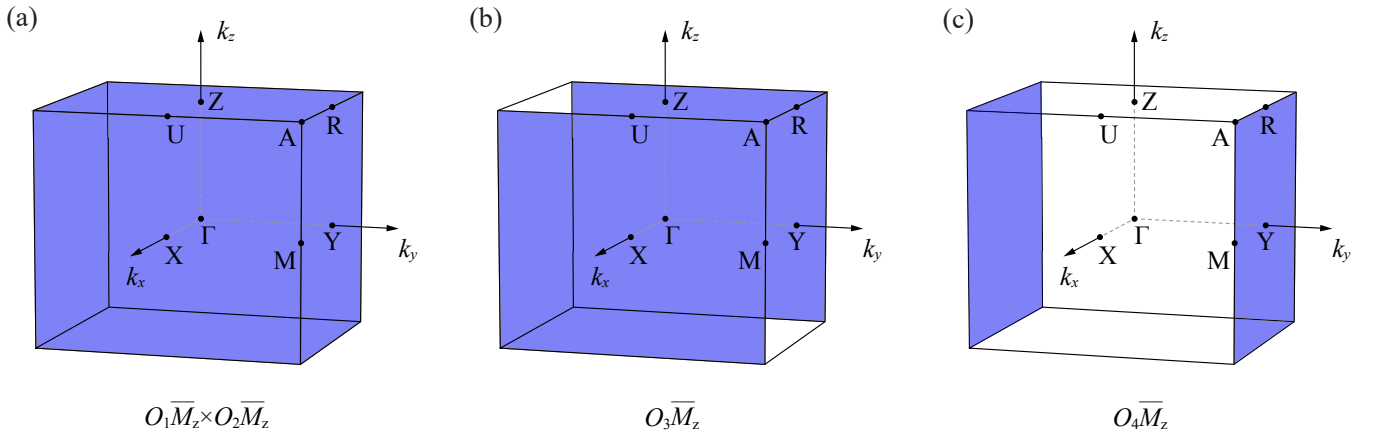


Figure 10. Double degeneracy of the electronic bands coupled to vertically stacked MX-II states. Blue shades mark the double degeneracy protected by the corresponding symmetries.

The double degeneracy along the BZ boundary $\mathbf{k} = (\pi/L, k_y)$ is protected by O_3 , where L is the lattice constant of the magnetic superlattice. Because $O_3^2 = e^{-ik_x L}$, O_3 becomes an antiunitary operator at $k_x = \pi/L$ where $O_3^2 = -1$. Moreover $\mathbf{k} = (\pi/L, k_y)$ is invariant under the action of O_3 that changes $(k_x, k_y) \rightarrow (-k_x, k_y)$. Therefore, there is a Kramers degeneracy of energy bands along the BZ boundary $\mathbf{k} = (\pi/L, k_y)$ [see Fig. 9(b)]. This symmetry can be broken by a net magnetization along y direction.

For the same reason, the double degeneracy along the BZ boundary $\mathbf{k} = (k_x, \pi/L)$ is protected by O_4 [see Fig. 9(c)]. This symmetry can be broken by a net magnetization along x direction.

We can further generalize the analysis to three-dimensional (3D) systems, where we couple electrons to vertically stacked MX-II states. Similarly to the 2D case, there are four relevant symmetries at zero field: $\{O_1 \bar{M}_z, O_2 \bar{M}_z, O_3 \bar{M}_z, O_4 \bar{M}_z\}$, where \bar{M}_z is the space reflection under which $z \rightarrow -z$.

These symmetries protect the band degeneracy at different parts of the 3D BZ:

1. $O_1 \bar{M}_z$ and $O_2 \bar{M}_z$ together protect the double degeneracy

of all energy bands over the whole BZ. The combined symmetries can be broken by a net magnetization or magnetic field in any direction [Fig. 10(a)].

2. $O_3 \bar{M}_z$ protects the double degeneracy of energy bands over the BZ surface at $\mathbf{k} = (\pi/L, k_y, k_z)$. This symmetry can be broken by a net magnetization or magnetic field along y direction [Fig. 10(b)].
3. $O_4 \bar{M}_z$ protects the double degeneracy of energy bands over the BZ surface at $\mathbf{k} = (k_x, \pi/L, k_z)$. This symmetry can be broken by a net magnetization or magnetic field along x direction [Fig. 10(c)].

Now we consider a transverse field in the y direction that induces a net magnetization in the same direction and breaks the $O_1 \bar{M}_z$, $O_2 \bar{M}_z$, and $O_3 \bar{M}_z$ symmetries. According to the analysis above, the remaining $O_4 \bar{M}_z$ symmetry protects the double degeneracy of the energy bands only at the surface of the BZ: $\mathbf{k} = (k_x, \pi/L, k_z)$ [Fig. 10(c)]. Further inclusion of the

spin-orbit coupling in the interlayer hopping

$$\begin{aligned}
& t_z \sum_i \sum_{\alpha\beta} \left(c_{i+\hat{z},\alpha}^\dagger \sigma_{\alpha\beta}^x c_{i,\beta} + h.c. \right) \\
&= \sum_{k_z} 2t_z \cos(k_z) \sum_{\alpha\beta} \sum_{\gamma} c_{k_z,\gamma,\alpha}^\dagger \sigma_{\alpha\beta}^x c_{k_z,\gamma,\beta}, \quad (\text{F5})
\end{aligned}$$

breaks the $O_4\overline{M}_z$ symmetry (γ is the index that labels different sublattices of the magnet supercell). However, Eq. (F5)

vanishes at $k_z = \pm\pi/2$ resulting in two nodal lines at $\mathbf{k} = (k_x, \pi/L, \pm\pi/2)$ [Fig. 6(a) in the main text].

To further reduce the nodal lines to Weyl points, we also include spin-orbit coupling in the intralayer hopping,

$$t_x \sum_i \sum_{\alpha\beta} \left(c_{i+\hat{x},\alpha}^\dagger \sigma_{\alpha\beta}^x c_{i,\beta} + h.c. \right), \quad (\text{F6})$$

which leads to the Weyl points shown in Fig. 6(b) in the main text.

-
- [1] H. Helmholtz, *The London, Edinburgh, and Dublin Philosophical Magazine and Journal of Science* **33**, 485 (1867), <https://doi.org/10.1080/14786446708639824>.
- [2] W. Thomson, *The London, Edinburgh, and Dublin Philosophical Magazine and Journal of Science* **34**, 15 (1867), <https://doi.org/10.1080/14786446708639836>.
- [3] T. H. R. Skyrme, *Proc. R. Soc. A* **260**, 127 (1961).
- [4] T. H. R. Skyrme, *International Journal of Modern Physics A* **3**, 2745 (1988).
- [5] F. Wilczek, “Beautiful losers: Kelvin’s vortex atoms,” (2011).
- [6] A. N. Bogdanov and D. A. Yablonskii, *Zh. Eksp. Teor. Fiz.* **95**, 178 (1989), [*Sov. Phys. JETP* **68**, 101 (1989)].
- [7] I. Dzyaloshinsky, *J. Phys. Chem. Solids* **4**, 241 (1958).
- [8] T. Moriya, *Phys. Rev. Lett.* **4**, 228 (1960).
- [9] S. Mühlbauer, B. Binz, F. Jonietz, C. Pfleiderer, A. Rosch, A. Neubauer, R. Georgii, and P. Böni, *Science* **323**, 915 (2009).
- [10] S.-Z. Lin, A. Saxena, and C. D. Batista, *Phys. Rev. B* **91**, 224407 (2015).
- [11] K. Karube, J. S. White, N. Reynolds, J. L. Gavilano, H. Oike, A. Kikkawa, F. Kagawa, Y. Tokunaga, H. M. Rønnow, Y. Tokura, and Y. Taguchi, *Nature Materials* **15**, 1237 (2016).
- [12] X. Z. Yu, W. Koshibae, Y. Tokunaga, K. Shibata, Y. Taguchi, N. Nagaosa, and Y. Tokura, *Nature* **564**, 95 (2018).
- [13] T. Kurumaji, T. Nakajima, V. Ukleev, A. Feoktystov, T.-h. Arima, K. Kakurai, and Y. Tokura, *Phys. Rev. Lett.* **119**, 237201 (2017).
- [14] T. Kurumaji, T. Nakajima, A. Feoktystov, E. Babcock, Z. Salhi, V. Ukleev, T. Arima, K. Kakurai, and Y. Tokura, “Direct observation of cycloidal spin modulation and field-induced transition in néel-type skyrmion-hosting vse_{205} ,” (2019), [arXiv:1912.06309 \[cond-mat.str-el\]](https://arxiv.org/abs/1912.06309).
- [15] N. D. Khanh, T. Nakajima, X. Yu, S. Gao, K. Shibata, M. Hirschberger, Y. Yamasaki, H. Sagayama, H. Nakao, L. Peng, K. Nakajima, R. Takagi, T.-h. Arima, Y. Tokura, and S. Seki, *Nature Nanotechnology* **15**, 444 (2020).
- [16] C. Zener, *Phys. Rev.* **81**, 440 (1951).
- [17] J. Stajic, *Science* **365**, 1260 (2019), <https://science.sciencemag.org/content/365/6459/1260.3.full.pdf>.
- [18] T. Okubo, S. Chung, and H. Kawamura, *Phys. Rev. Lett.* **108**, 017206 (2012).
- [19] A. O. Leonov and M. Mostovoy, *Nat. Commun.* **6**, 8275 (2015).
- [20] S.-Z. Lin and S. Hayami, *Phys. Rev. B* **93**, 064430 (2016).
- [21] S. Hayami, S.-Z. Lin, and C. D. Batista, *Phys. Rev. B* **93**, 184413 (2016).
- [22] C. D. Batista, S.-Z. Lin, S. Hayami, and Y. Kamiya, *Rep. Prog. Phys.* **79**, 084504 (2016).
- [23] S. Gao, H. D. Rosales, F. A. Gómez Albarracín, V. Tsurkan, G. Kaur, T. Fennell, P. Steffens, M. Boehm, P. Čermák, A. Schneidewind, E. Ressouche, D. C. Cabra, C. Rüegg, and O. Zaharko, *Nature* **586**, 37 (2020).
- [24] Z. Wang, Y. Su, S.-Z. Lin, and C. D. Batista, *Phys. Rev. Lett.* **124**, 207201 (2020).
- [25] S. D. Yi, S. Onoda, N. Nagaosa, and J. H. Han, *Phys. Rev. B* **80**, 054416 (2009).
- [26] J. P. Chen, D.-W. Zhang, and J.-M. Liu, *Scientific Reports* **6**, 29126 (2016).
- [27] Y. Kamiya and C. D. Batista, *Phys. Rev. X* **4**, 011023 (2014).
- [28] Z. Wang, Y. Kamiya, A. H. Nevidomskyy, and C. D. Batista, *Phys. Rev. Lett.* **115**, 107201 (2015).
- [29] S.-S. Zhang, H. Ishizuka, H. Zhang, G. B. Halász, and C. D. Batista, *Phys. Rev. B* **101**, 024420 (2020).
- [30] L. N. Bulaevskii, C. D. Batista, M. V. Mostovoy, and D. I. Khomskii, *Phys. Rev. B* **78**, 024402 (2008).
- [31] R. Ramazashvili, *Phys. Rev. Lett.* **101**, 137202 (2008).
- [32] N. P. Armitage, E. J. Mele, and A. Vishwanath, *Rev. Mod. Phys.* **90**, 015001 (2018).
- [33] P. Puphal, V. Pomjakushin, N. Kanazawa, V. Ukleev, D. J. Gawryluk, J. Ma, M. Naamneh, N. C. Plumb, L. Keller, R. Cubitt, E. Pomjakushina, and J. S. White, *Phys. Rev. Lett.* **124**, 017202 (2020).
- [34] X. Wan, A. M. Turner, A. Vishwanath, and S. Y. Savrasov, *Phys. Rev. B* **83**, 205101 (2011).
- [35] A. A. Burkov and L. Balents, *Phys. Rev. Lett.* **107**, 127205 (2011).
- [36] R. Ozawa, S. Hayami, K. Barros, G.-W. Chern, Y. Motome, and C. D. Batista, *J. Phys. Soc. Jpn.* **85**, 103703 (2016).
- [37] R. Ozawa, S. Hayami, and Y. Motome, *Phys. Rev. Lett.* **118**, 147205 (2017).
- [38] S. G. Johnson, “The nlopt nonlinear-optimization package,” [Http://github.com/stevengj/nlopt](http://github.com/stevengj/nlopt).